The Journal of Chemical Physics

Insight into hydrogen production through molecular simulation of an electrode-ionomer electrolyte system

Cite as: J. Chem. Phys. **151**, 034702 (2019); https://doi.org/10.1063/1.5097609
Submitted: 26 March 2019 . Accepted: 24 June 2019 . Published Online: 16 July 2019

R. E. Jones, W. C. Tucker, M. J. L. Mills, and S. Mukerjee

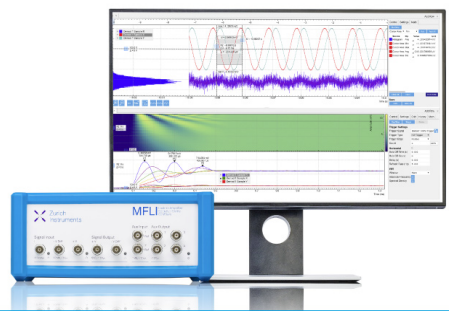

The Journal of Chemical Physics ARTICLE scitation.org/journal/jcp

Insight into hydrogen production through molecular simulation of an electrode-ionomer electrolyte system

Cite as: J. Chem. Phys. 151, 034702 (2019); doi: 10.1063/1.5097609
Submitted: 26 March 2019 • Accepted: 24 June 2019 •
Published Online: 16 July 2019

R. E. Jones,[1,a] W. C. Tucker,[1] M. J. L. Mills,[1] and S. Mukerjee[2]

AFFILIATIONS

[1]Sandia National Laboratories, Livermore, California 94551, USA
[2]Northeastern University, Boston, Massachusetts 02115, USA

[a]Electronic mail: rjones@sandia.gov

ABSTRACT

In this work, we examine metal electrode-ionomer electrolyte systems at high voltage (negative surface charge) and at high pH to assess factors that influence hydrogen production efficiency. We simulate the hydrogen evolution electrode interface investigated experimentally in the work of Bates *et al.* [J. Phys. Chem. C **119**, 5467 (2015)] using a combination of first principles calculations and classical molecular dynamics. With this detailed molecular information, we explore the hypotheses posed in the work of Bates *et al.* In particular, we examine the response of the system to increased bias voltage and oxide coverage in terms of the potential profile, changes in solvation and species concentrations away from the electrode, surface concentrations, and orientation of water at reactive surface sites. We discuss this response in the context of hydrogen production.

https://doi.org/10.1063/1.5097609

I. INTRODUCTION

Hydrogen has the capacity to be an ecologically friendly fuel since water is the primary by-product of its use. Many technological and economic challenges remain in realizing a viable hydrogen economy and energy system.[1,2] The central issue is that molecular hydrogen gas does not occur naturally in abundance and must be produced industrially. Currently, the majority of hydrogen is generated by either high-temperature/high-energy methane reforming or the water-gas shift reaction which produces significant carbon dioxide, while the electrolysis of water accounts for a relatively minor proportion of hydrogen production.[3] As electrolysis is not directly dependent on fossil fuels, there is strong motivation to develop a low cost, low energy electrolytic process. Since electrolysis traditionally depends on expensive Pt-group catalysts, transition metal catalysts are being developed.

Mukerjee and co-workers have been developing Ni based catalysts with ionomer-based electrolytes[4,5] which show promise but are still confronted by development challenges in part due to the need for a more fundamental understanding of the electrode-electrolyte interaction. In the work of Bates *et al.*,[4] a number of hypotheses were put forward:

H1. The electrical potential is significantly altered by the ionomer. The ionomer extends the "electrified interface" near the catalyst. The potential at the inner Helmholtz plane (IHP) dictates the rate of the hydrogen evolution reaction (HER). This potential is more positive than it would be in absence of ionomer and this affects the reactant water molecules at the inner plane.
H2. The ionomer itself straddles the inner and outer Helmholtz planes (OHP) and is directly chemisorbed on the metal surface.
H3. The majority of the metal surface is coordinated with water molecules.
H4. The water molecules inside the inner Helmholtz plane orient with dipoles pointing away from the electrode due to the presence of the ionomer, and this facilitates H–OH cleavage on the metal catalyst.

H5. Nanoscale heterogeneity provides a high density of adjacent metal/metal-oxide sites where metallic Ni has an affinity for H-bonding, and NiO_x has an affinity for adsorbed OH^-, in-line with Markovic's theory of enhanced hydrogen evolution reaction on composite metal/metal-oxide surfaces.[6–8]

In this work, we investigate these hypotheses via molecular simulation. Since a system encompassing the compact and diffuse layers of the long chain ionomer-based electrolyte is too large for *ab initio* calculations such as Refs. 9–17, which allow charge transfer and spontaneous dissociation, we employ classical molecular dynamics (MD) to model the system at the relevant length and time scales. Note that reactive empirical potentials, such as ReaxFF,[18] are also infeasible in the present context, in part due to the inability to model the charging and oxides of the electrode and the bonding states of the ionomer, as well as their computational cost. Water-metal interfaces have been studied with MD for some time.[19–27] The absence of chemical reactions in these simulations is offset by the fact that these reactions are fast compared to diffusion time scales resolvable with MD and we prepopulate the simulation with the relevant chemical species. We assume that simulations of the isothermal steady-state accounting for electrostatic and steric interactions with the experimentally observed species concentrations are informative of the transport-limited steady operation of the actual cell. Also, we apply *ab initio* methods to assess the near electrode charge environment and use this information in the MD model of the electrode. We focus on the hydrogen evolution reaction (HER) environment at the negatively charged electrode (cathode). Here, the ionomer is in contact with bare metal (Ni) and metal oxide (NiO_x) at the electrode surface. The ionomer-based electrolyte has characteristics that differ from the well-studied dissolved salt electrolytes. For instance, the ionomer is relatively immobile due to its polymeric structure with fixed charge centers (N^+), while the counter ions (OH^-) are mobile. The influence of the immobile charge in ionomer strands/chains on performance is central to our investigation.

Given its importance, the structure and chemistry of water near a metal surface has a long and intense field of study in and of itself, which is reviewed in Refs. 28–32. The examination of the water-surface interactions has been pursued in great detail by combinations of microscopy and *ab initio* simulation (typically in vacuum), as in Ref. 33, and has led to many postulated and observed intact, partially dissociated, and fully dissociated configurations of water at uncharged atomically flat and rough surfaces. Despite the limitations of classical MD, we attempt to interpret the results of this study in the context of this deep body of research.

In Sec. II, we briefly review the relevant theory. With representative electrode-ionomer systems, we simulate the response of these systems to a range of external electrical bias and characterize this response by a variety of means to address the hypotheses of Bates *et al.*[4] In Sec. III, we describe how we use spatial resolution of charge density, per-species radial distributions, and other fields to quantify the location of the Helmholtz planes and significant concentrations of the reactive species. The results are given in Sec. IV and are discussed in Sec. V in light of the hypotheses of Bates *et al.*[4]

II. THEORY

Due to high electric fields near electrodes, charged mobile species tend to pack and form characteristic structures and concentration profiles. This phenomenon is modeled in the classical theory by Helmholtz,[34] Gouy,[35] Chapman,[36] Stern,[37] and others, and is still a topic of current research.[38] Here, we will briefly review the relevant theory to assist in interpreting the molecular results in Sec. IV.

The most commonly used theory is the Gouy-Chapman-Stern (GCS) model, composed of a compact layer of ions next to the electrode and a diffuse layer beyond. The compact layer is bounded by the inner Helmholtz plane (IHP) at a layer of unsolvated ions adsorbed on the electrode surface and the outer Helmholtz plane (OHP) where ions are fully solvated. The interior of the compact layer is assumed to be charge free due to steric effects. The structure of the diffuse layer is governed by the Poisson-Boltzmann (PB) equation where the electrostatic interaction of the ions is given by the Poisson equation,

$$-\nabla\cdot(\epsilon\nabla\phi)=\rho. \tag{1}$$

Here, ϕ is the electric potential and ϵ is the electric permittivity. The net charge density ρ is given by

$$\rho = e\sum_a z_a c_a, \tag{2}$$

where z_a is the valence of species a, c_a is its concentration, and e is the unit of elemental charge. In equilibrium, the absence of fluxes implies that both the electrochemical potential, $ez_a\phi + k_BT\ln c_a$, and the temperature, T, are constant across the system domain. This condition leads to species concentrations, c_a, that vary with the local potential ϕ,

$$c_a = \bar{c}_a \exp\left(\frac{ez_a\phi}{k_BT}\right), \tag{3}$$

where $\bar{c}_a$ is the far-field/bulk concentration of species a. Substituting Eqs. (2) and (3) in Eq. (1) results in the Poisson-Boltzmann (PB) equation. The characteristic thickness of the diffuse layer is given by the Debye length

$$\lambda_D = \sqrt{\frac{k_BT\epsilon}{e^2\sum_a z_a^2\bar{c}_a}}, \tag{4}$$

which is the similarity parameter in the solution of the linearized PB equations. For more details, see Ref. 39 (Sec. 13.3), Ref. 40 (Chap. 12), and Ref. 41 (Sec. 7.4).

Real electrode-electrolyte systems deviate from GCS for a number of reasons such as finite ion size and correlation effects due to van der Waals interactions and a nonuniform dielectric field due to varying concentration and discrete charges.[42–44] Also, theoretical concepts such as full solvation and the location of Helmholtz planes become less well-defined. In the present case, an electrolyte with a dense ionomer, the charge centers of ionomer chains are effectively immobile and a simple model assumes that these ionomer charges provide a background charge density which is fully solvated and screened far from the electrode. Consequently, the PB equation governs the excess charge of the counter ion. This paradigm holds where counter ions stay bound to ionomer charge centers and fails where

the electric field is strong enough to dissociate the mobile species from the charge centers. The solution to the PB equation for the counter ions only[45] is

$$\phi(x) = -2\frac{k_B T}{e}\ln\left(1+\frac{x}{\ell}\right)+\phi_0 \tag{5}$$

and

$$c(x) = \frac{c_0}{\left(1+\frac{x}{\ell}\right)^2}, \tag{6}$$

where ϕ_0 is the potential at $x = 0$, $\ell = 2\frac{\epsilon k_B T}{e\sigma}$, and σ is the surface charge of the electrode. Note that the dielectric of the electrolyte, ϵ, is assumed to be spatially uniform in this derivation. This diffuse layer solution has an electric field $\mathbf{E} = -\nabla\phi$ that is zero far away from the electrode and has the magnitude $\frac{\sigma}{\epsilon}$ at $x = 0$, which is consistent with Gauss's law applied to the electrode (this discussed in more detail in Sec. III).

III. METHOD

To simulate the metal electrode-ionomer based electrolyte system, we employ a combination of density functional theory (DFT) and classical molecular dynamics (MD). We use DFT to determine the charge state of the metal HER electrode, which is our primary focus. We use MD to model the dynamics of the molecular species of the electrolyte through interplay of electrostatic, elastic, steric, and diffusion forces in the overall system. By its explicit representation of atoms and atomic bonding, MD is known to capture deviations from classical theories such as GCS[46–48] but does not model reactions involving charge transfer or breaking/forming of covalent bonds.

In the molecular model, the electrode-electrolyte system atoms and molecules interact with each other via the well-known CHARMM empirical potential.[49] This often employed potential depends on atomic charges and proximity. It is composed of short-range van der Waals interactions, long-range Coulomb interactions, and intramolecular covalent bonds,

$$\Phi(\mathbf{x}_\alpha) = \underbrace{\sum_{\alpha<\beta} 4\varepsilon_{ab}\left(\left(\frac{\sigma_{ab}}{r_{\alpha\beta}}\right)^{12}-\left(\frac{\sigma_{ab}}{r_{\alpha\beta}}\right)^{6}\right)}_{\text{van der Waals}}+\underbrace{\frac{1}{4\pi\epsilon_0}\sum_{\alpha<\beta}\frac{q_\alpha q_\beta}{r_{\alpha\beta}}}_{\text{Coulomb}}$$
$$+\underbrace{\sum_I\left[\sum_{\alpha,\beta\in M_I} k_{ab} r_{\alpha\beta}^2+\sum_{\alpha,\beta,\gamma\in M_I} k_{abc}\theta_{\alpha\beta\gamma}^2+\sum_{\alpha,\beta,\gamma,\mu\in M_I} k_{abcd}\phi_{\alpha\beta\gamma\mu}^2\right]}_{\text{covalent}}, \tag{7}$$

where ε_{ab} and σ_{ab} are the usual Lennard-Jones (LJ) pair parameters for species a and b, q_α is the charge of atom α, $r_{\alpha\beta} = \|\mathbf{x}_\alpha - \mathbf{x}_\beta\|$ is the distance between atoms α and β, and a, b, c, d index atom types. We employ a particle-particle particle-mesh (PPPM) solver[50] to efficiently compute the long-range Coulomb interactions with a short/long cutoff of 12 Å. Here, the permittivity of free space is $\varepsilon_0 = 0.005\,526\,35e/\text{V Å}$. The intramolecular bonds are affected by harmonic potentials based on pair distances $r_{\alpha\beta}$, 3 atom angles $\theta_{\alpha\beta\gamma}$, and 4 atom dihedral angles $\phi_{\alpha\beta\gamma\mu}$, where M_I is a set of like molecules.

A. Electrode

Given the form of the interatomic potential, Eq. (7), which includes Coulomb forces, we need the point charges q_α for the classical representation of the electrode via Eq. (7) and the response of the electrode point charges to electrical bias/external potential V. We use DFT with Perdew, Burke, Ernzerhof (PBE)/Generalized Gradient Approximation (GGA) level of theory[51] to obtain relaxed surface structures and compute point charges via a Bader analysis of the charge density field.[52]

Since only studies of small systems are feasible with DFT, we examined specific domains of a partially oxidized Ni electrode: bare Ni, partially oxidized Ni, and Ni covered by an NiO layer. For each, we create a small, laterally periodic system to calculate charge density using a fcc unit cell with a 3.52 Å lattice constant for Ni regions and a cubic B1 unit cell with a 4.17 Å lattice constant for NiO regions. We select (100)-oriented (nonpolar) surfaces for both Ni and NiO. The surfaces neighbor vacuum regions, not representative electrolytes, for simplicity and under the assumption that the proximity of the electrolyte evokes only perturbations of the charge density. We employ an energy cutoff of 500 eV for the metallic systems and 800 eV for the systems containing oxides, together with an $8 \times 8 \times 1$ Γ centered k-point grid. After computing a baseline charge density, we add excess electrons to emulate negative charging of the electrode of interest. Finally, we obtain the electrode point charges $q'_\alpha(\sigma)$,

$$q'_\alpha(\sigma) = q_\alpha - \frac{\sigma}{e\eta}\Delta q_\alpha, \tag{8}$$

where q_α are the baseline point charges (such that $\sum_\alpha q_\alpha = 0$), Δq_α are the perturbed point charges (corrected for the homogeneous background charge and normalized such that $\Delta q_\alpha = 1\ e$ for the surface atoms), σ is the target surface charge density, and η is the surface atom density. The number of excess electrons added to the systems to obtain the perturbed charge field is on the order of $0.1e$ per surface atom and on par with the perturbation needed to achieve the voltage bias V in the range $V \approx 0$–2.5 V in the experimental system. Finally, the scaling of Eq. (8) with external voltage V follows $V \approx \frac{\lambda_D}{\varepsilon_0}\sigma$; however, we recover the actual voltage in the MD systems via a Gauss box method described in Sec. III.

In addition to the point charges required for Coulomb interactions, short-range parameters ε_{ab} and σ_{ab} for the electrode interactions with the ionomer are needed. By assuming traditional Lorentz-Berthelot mixing, only the LJ self-self pair parameters are required. We obtain these from published, surface specific parameterizations: for Ni, $\sigma_{\text{NiNi}} = 2.274$ Å and $\epsilon_{\text{NiNi}} = 5.65$ kcal/mol Ref. 53 (Table 1) and for NiO, $\sigma_{\text{OO}} = 1.292$ Å and $\epsilon_{\text{OO}} = 35.62$ kcal/mol Ref. 54 (Table 1).[55] For simplicity (since no additional parameters are needed) and

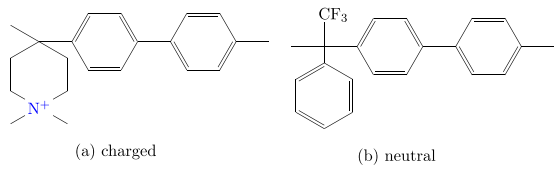

FIG. 1. PAP-DP-60 ionomer units: (a) charged (60%) and (b) neutral units (40%). The ionomer is charge balanced by OH^-.

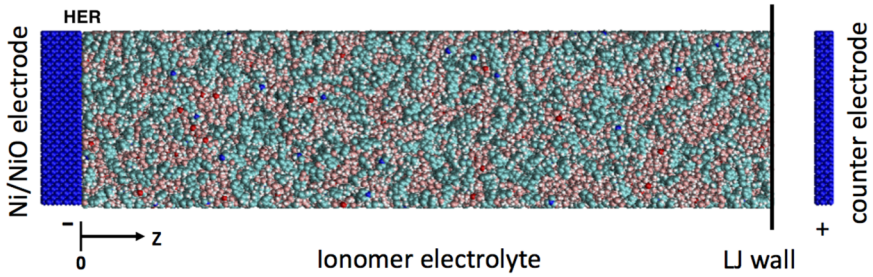

FIG. 2. Electrode:electrolyte system. The ionomer membrane infused with OH^- counter ions and water. The metal electrode has imposed surface charges to effect electrical bias. The replica systems have dimensions: 6–7 nm × 6–7 nm × 34–38 nm each consisting of 32 unique ionomer chains with random sequences. The origin $z = 0$ is a plane through centers of the surface layer atoms of the Ni/NiO (HER) electrode.

efficiency, we neglect thermal motion of the electrode and fix the locations of its Ni and O atoms.

B. Electrolyte

The selected ionomer (PAP-DP-60) is an amorphous material composed of long polymer chains with N^+ charge centers charge-balanced by OH^- together with water. Each chain is composed of charged (c) and neutral units (n), see Fig. 1, in a ratio c:n = 60:40 with lengths of 30–40 units in a random sequence. The mass density of the ionomer is 1.1 g/cm^3 with about 40% water by weight at room temperature and pH in the range 13–14+.

Using these experimental measurements, we created representative models of the ionomer electrolyte; see Fig. 2. First, we created chains from the units using a random sequence that respected the experimental bounds on length and c:n ratio. Next, we added molecular water and OH^- ions. To achieve the experimentally measured density, we compressed the ionomer-electrolyte mixture and then relaxed the compressed configuration at 2000 K via isothermal dynamics to relieve unphysical local configurations for 0.4 ns. Finally, we cooled the system to 300 K at 10 K/ps and let it equilibrate for 0.1 ns. To complete the electrode-electrolyte system seen in Fig. 2, we added the primary Ni electrode plus a soft wall and counter electrode to bound the system. The separation of the capping wall and the counter electrode was expedient due to different densities and lengths of the replicas while maintaining the same effective gradient in external potential. Due to computational cost, we can only place the counter electrode 400 nm from the surface of the primary electrode. As stated in the Introduction, our focus is on the Ni electrode where the HER occurs and, hence, we model it in detail and simplify the counter electrode. For our purposes, this is sufficient as long as the diffuse layer near the primary electrode relaxes to the bulk, and the region away from the primary electrode is not depleted of mobile species. As we will see in Sec. IV, both these conditions are satisfied. Also, in preliminary studies, the lateral dimensions of the systems were increased to the point where the charge density profiles and related measures converged to within the expected statistical noise.

Since the ionomer is amorphous, we generated a number of statistically equivalent replica systems to improve sampling and reduce finite size effects. The isothermal dynamics of the electrolyte were evolved with a Nosé-Hoover algorithm which accommodated the rigidity of the intramolecular bonds. All reported results are the average of 8 configurations time-averaged and simulated for 0.4 ns each with a 1 fs time step.

Finally, we use a so-called Gauss box to recover the electric potential ϕ from the point charges q_α. Briefly, starting with Gauss's law for a quasi-one dimensional system, with electric field $\mathbf{E} \equiv -\nabla\phi = E\mathbf{e}_3$ and cross-sectional area A, we obtain

$$\phi(z) = \phi(0) - \frac{1}{\varepsilon_0 A}\int_0^z \overbrace{\Big\langle \sum_{\alpha|z_\alpha\in[0,\tilde{z}]} q_\alpha \Big\rangle}^{Q(\tilde{z})}\, d\tilde{z}, \tag{9}$$

where $Q(\tilde{z})$ is the total/net charge in $z \in [0,\tilde{z}]$ and $\langle\bullet\rangle$ is the average over replica systems and steady-state trajectories in each system. In a similar fashion, we estimate charge density, dipole density, and species concentration profiles using coarse-grained point charges q_α, atomic dipoles $q_\alpha\mathbf{x}_\alpha$, and species type. For instance, the water dipole density is given by

$$\mu(z_I) = \frac{1}{V_I}\Big\langle \sum_\alpha q_\alpha z_\alpha w(z_I - z_\alpha)\Big\rangle - \frac{1}{V_I} q_I z_I, \tag{10}$$

where z_I is the location of points on the coarse-grained sampling grid, V_I is the effective volume associated with I, w is a partition-of-unity, tentlike kernel function, and

$$q_I = \Big\langle \sum_\alpha q_\alpha w(z_I - z_\alpha)\Big\rangle. \tag{11}$$

In Eq. (10), the second term is a correction for net charge in a particular bin I. Also, we use a kernel width of 3 Å based on the size of water molecules and cut off the averaging kernel $w(z)$ at the electrode surface so that the average only includes the time-dependent data in the electrode. The water dipole density is used to determine water orientation, and the species concentrations indicate which species are present in the compact and diffuse layers. Also, we extract coarse-grained profiles of radial distribution functions (RDFs) of particular species to quantify changes in solvation with 3 Å resolution. This information allows us to estimate the location of the OHP and its response to bias.

IV. RESULTS

We compare the response of the electrolyte to electrode bias voltage using a variety of configurational metrics in order to provide insight and support to the experimental hypotheses described in the Introduction. We focus on (a) bare Ni, (b) fully NiO covered, and (c) partially NiO covered regions of the Ni electrode. Figures 3 and 4 show the qualitative differences in the

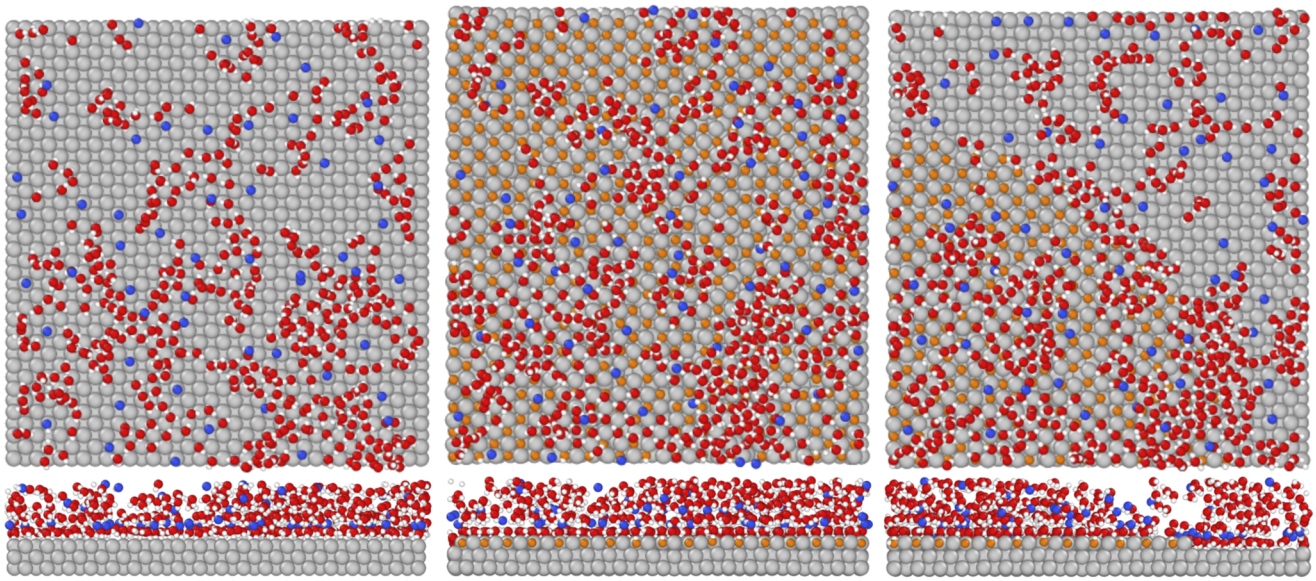

FIG. 3. Surface coverage of H_2O, OH^-, and N^+ in the ionomer for $q = -0.10e$/atom (top-down and side views of instantaneous configurations). (a) Bare Ni, (b) Ni covered by a monolayer of NiO, and (c) Ni with an ≈50% partial NiO coverage quarter disk monolayer centered on the lower left corner of the top view. Atom color map, H: white, O: red, N^+: blue, Ni: gray, O in NiO: orange.

surface coverage of the relevant species and water orientation for the three cases. Figures 3 and 4 will be discussed in more detail in Secs. IV A–IV C.

A. Electrode charge distributions

Using the first principles methods described in Sec. III A, we obtain the relaxed configuration and electron density of the electrode with and without an oxide layer. Figure 5 shows a top down view of the charge density of a Ni surface partially covered by a NiO monolayer. The NiO island is in the lower left of Fig. 5, and the exposed portion of the underlying Ni surface can be seen in the remainder of the figure. The initially square island relaxes to a more diamondlike shape, but the variation in charge density across the partial layer is minimal, with charge transfer from the O to Ni nuclei as expected. Also, the charge density of the exposed Ni metal

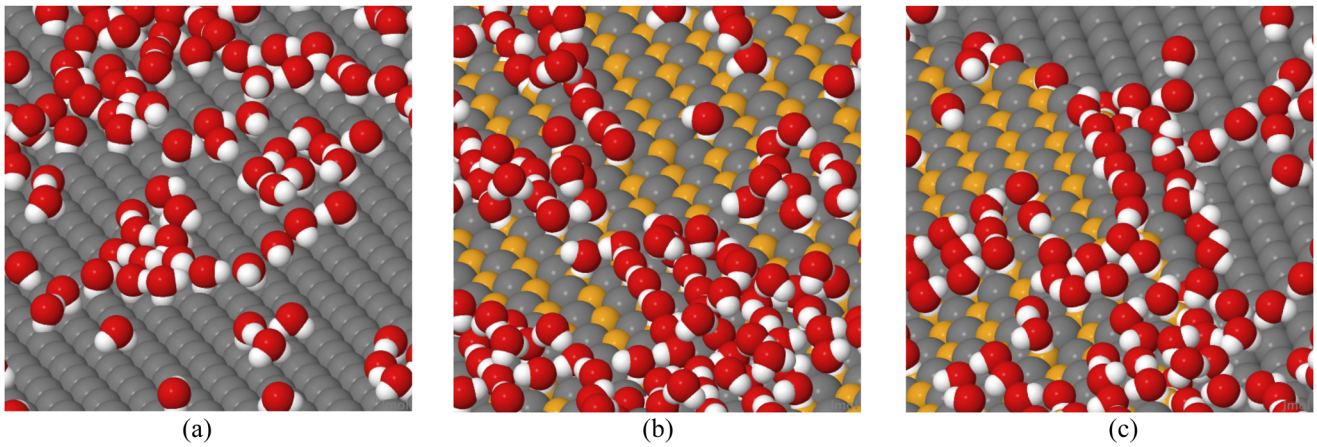

FIG. 4. Surface orientation of H_2O, for $q = -0.10e$/atom (instantaneous configurations). (a) Bare Ni, (b) Ni covered by a monolayer of NiO, (c) Ni with an ≈50% partial NiO coverage quarter disk monolayer centered on the lower left corner of the top view. Atom color map, H: white, O: red, N^+: blue, Ni: gray, O in NiO: orange.

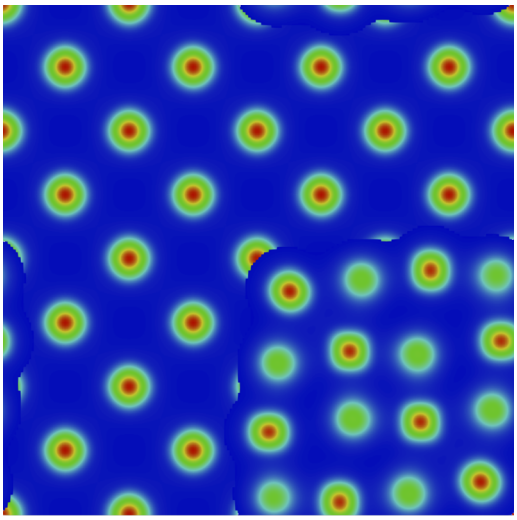

FIG. 5. Electrode charge density (top down view) in a region where a monolayer of NiO partially covers the Ni electrode (lower left). The cross section of the charge density of the partial NiO monolayer is superposed over the charge density of the underlying Ni surface.

is relatively unperturbed by the oxide layer. The mean separation between the Ni and the NiO layer is ≈2 Å. With a sequence of related simulations, we examined where the excess electrons (induced by electrode charging) reside. Figure 6 plots the point charges (in excess of normal valence: metal Ni 0, oxide Ni +2, O −2) for bare Ni and Ni covered by 1, 2, and 3 monolayers of NiO (the point charges for an overall neutral system and one with excess electrons are extracted with a Bader method described in Sec. III and then differenced). As expected, in the bare Ni, the excess electron density resides primarily in the outermost layer of Ni. For a single layer of NiO covering Ni, ≈80% of the excess electrons reside near the

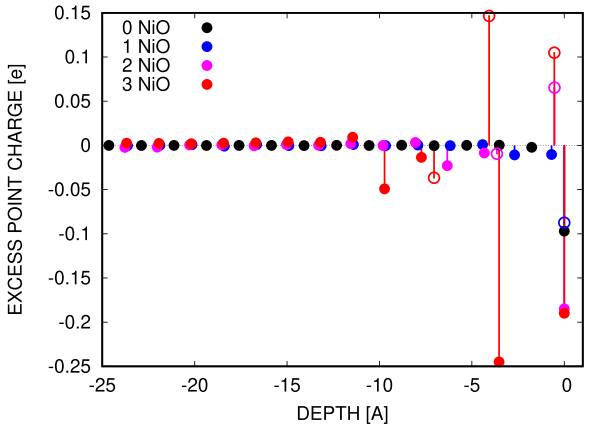

FIG. 6. Excess point charges in the electrode: (black) bare Ni region, region of NiO on Ni with (1) blue, (2) magenta, (3) red monolayers of NiO. Open circle marker: O, solid circle: Ni. Excess charge is relative to the expected valence, pure Ni: 0, and Ni: +2, and O: −2 in the oxide layer.

O, ≈10% near the Ni in the oxide layer, and ≈10% near the Ni in the underlying metal. This charge splitting induces a surface dipole moment. It is apparent that the charge distribution and the dipole effects become more complex as more oxide layers are added to the system.

B. Bare metal region of the electrode

With classical MD, we simulated the electrode-electrolyte systems over a sequence of surface charges: $\Delta q = \{0.0, 0.05, 0.10, 0.15\}e$ per surface atom, corresponding to $\sigma = \{0.007, 0.014, 0.021, 0.028\}e/\text{Å}^2$. These surface charges were related to voltage through the Gauss box technique described in Sec. III.

Figure 7 shows that the voltages at the electrode surface ($z = 0$) range from 0 to ≈2 V for these surface charges. Also, it is apparent from the charge density profiles that (a) both a double layer next to the electrode and a diffuse layer grading to the bulk form exist, and (b) the decay to the bulk region with zero net charge occurs within 20 Å from the outer layer of the electrode. The apparent complete screening of the surface charge by the mobile charges in the electrolyte indicates that the N^+ charge centers on the electrode-facing surface of the ionomer are capable of sufficient rearrangement (coupled with the depletion of the more mobile OH^- near the electrode) in response to the potential bias. We fit the potential profile in the diffuse region (approximately 5–20 Å from the electrode surface) to the Poisson-Boltzmann solution in Eq. (5) and obtain $\ell \approx 0.5$ Å for $q = -0.1e$/atom. This allowed us to estimate the effective dielectric in the diffuse layer $\epsilon = \frac{e\sigma}{2k_BT}\ell \approx 24.4\epsilon_0$ which is considerably less than pure water ($\epsilon \approx 80\epsilon_0$).

In Fig. 7, we also see that the region of significant dipole moment near the electrode decays to the bulk on the same scale as the potential that induces the orientation of the water molecules

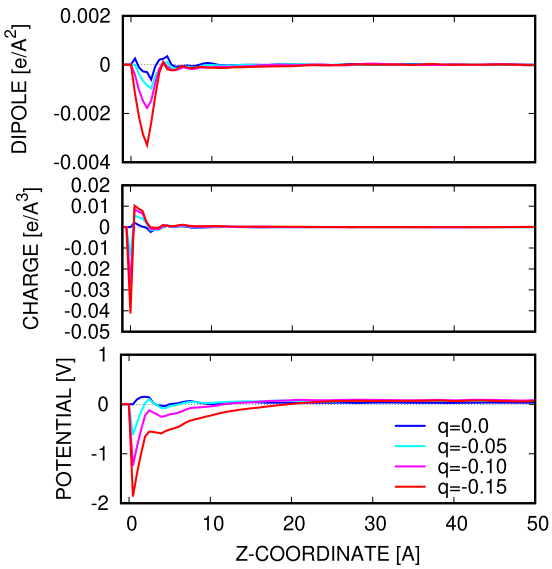

FIG. 7. Bare Ni electrode: electrostatic potential, charge, and water dipole density profiles as a function of surface charge q (e/atom) on the electrode.

seen in Figs. 3 and 4. Significantly, the dipole moment is mostly negative and increases in magnitude with applied bias, which corresponds to the expected conformation of the H atoms of the water molecules oriented closest to the negative electrode, and this orientation becomes more dominant with increased bias. This finding is corroborated by direct observation, as in Figs. 3 and 4 (at $q = -0.1e$/atom), where the white, partially positively charged H atoms lie on the electrode surface with the red, partially negatively charged O atoms of the same water molecules pointing away from the surface. Either one or both hydrogens are directly associated with distinct metal surface atoms. In a second layer, we observe some water molecules bridging water on the surface with their hydrogens associated with the oxygens of the surface adsorbed waters. Even at zero bias, it appears that there is some orientational preference for the water molecules which must be induced by the particular LJ parameters for H and O atoms in the water molecules. (The preferential alignment of water with uncharged surfaces is widely observed.[31])

Figure 8 shows that at zero bias, H_2O, OH^-, and the N^+ of the ionomer are adsorbed to the electrode surface and maintain uniform bulk concentrations away from the electrode. At higher biases, OH^- is excluded near the electrode, and water fills the vacated region and forms structured layers. The spatial distribution of N^+ (averaged over time and the replica systems) is effectively uniform in the electrolyte region except there is a significantly higher concentration of N^+ at the interface (with corresponding neighboring region of depletion). This appears to be due to the fact that ends of the chains are relatively mobile, unentangled, and attracted to the surface of the negative electrode. The concentration of N^+ at the electrode more than doubles with the applied bias of ≈2 V, and the response appears to be nonlinear, most likely due to an energy barrier in straightening the ends of the ionomer chains. This can be seen as competition

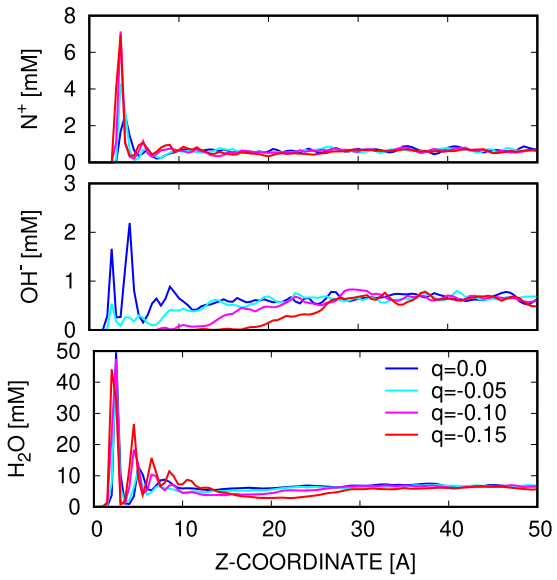

FIG. 8. Bare Ni electrode: N^+, OH^-, and H_2O density profiles as a function of surface charge q (e/atom) on the electrode.

of elastic vs Coulomb forces for the relatively immobile N^+. Note that these biases are high enough to dissociate water in the real system and the ionomer near the electrode might be likewise affected. The mobile species, H_2O and OH^-, respond as mentioned. From Fig. 3, it is apparent that no ringlike water structures form and that, generally, the N^+ of the ionomer appear in regions of low concentrations of surface adsorbed water. We presume that the near surface N^+ of the ionomer displace water and disrupt the tendency for the water to form regular structures. The OH^- transitions from significant surface adsorbed species at no bias to progressively vacated regions with increased voltage. Here again, a threshold (determined by the relative magnitude of the overall electric field separating OH^- and N^+ vs the LJ and Coulomb forces binding them) appears to be operating. For biases less than $q = -0.05e$/atom (not shown), OH^- remains bound to N^+. Note that effectively no OH^- is present near the electrode at $q = -0.10e$/atom surface charge shown in Fig. 5(a). Water, on the other hand, displays a surface adsorbed layer, a depletion zone, and then a uniform bulk concentration at no bias. With increasing voltage, more structured water layers appear near the surface and the closest layer becomes more packed (higher surface coverage).

Figure 9 shows the spatially binned RDFs for zero bias and $q = -0.10e$/atom. First of all, we see that OH^- is closely coordinated with H_2O and this strong association does not change wherever OH^- is present. At voltage, the only effect is decreasing the magnitude (not the location) of the RDF peak due to decreased OH^- concentration near the electrode surface (refer to Fig. 8). Note that no OH^- is present at 0–6 Å from the electrode at $q = -0.10e$/atom. The coordination of N^+ with H_2O is uniform at zero bias and relatively unaffected at high bias which implies that the OHP defined by H_2O solvation of N^+ is within 3 Å of the outer layer of the electrode surface. The effects of distance from the electrode and bias on the coordination of N^+ with OH^- are more complex due to changing local electric field and concentration. Given the location of the RDF peaks, the primary coordination shell of OH^- appears to mix with that of H_2O. Most significant of the changes is that N^+ coordination with OH^- tightens and sharpens at high bias and near the electrode, particularly in the 6–9 Å bin at $q = -0.1e$/atom. In the next bin, 9–12 Å, we see two peaks corresponding to a two shell arrangement; in the 15–18 Å bin, the RDF resembles that of the bulk in both the zero and high bias cases. If we use the coordination of N^+ with OH^- to indicate the location of the OHP, we see the OHP shift away from the electrode surface reaching ≈20 Å at the highest bias, as Fig. 8 indicates, due to the dissociation of the OH^- from the N^+ at high bias.

C. Oxide covered region of the electrode

As observed in Figs. 3 and 4, the presence of a (single layer of) NiO qualitatively changes the response of the HER electrode to electrical bias. Comparing the surface coverage of a bare Ni region of the electrode with partially and fully covered NiO regions, we see approximately 40% increase of adsorbed water where there is oxide on the surface. Figure 3 also illustrates that there is distinctly increased water surface concentration at the NiO boundary. The side view of the electrode in Fig. 3 and the close-up in Fig. 4 show water molecules on the surface of the NiO covered electrode with one of the O–H legs of the water molecule flat on the surface and the other

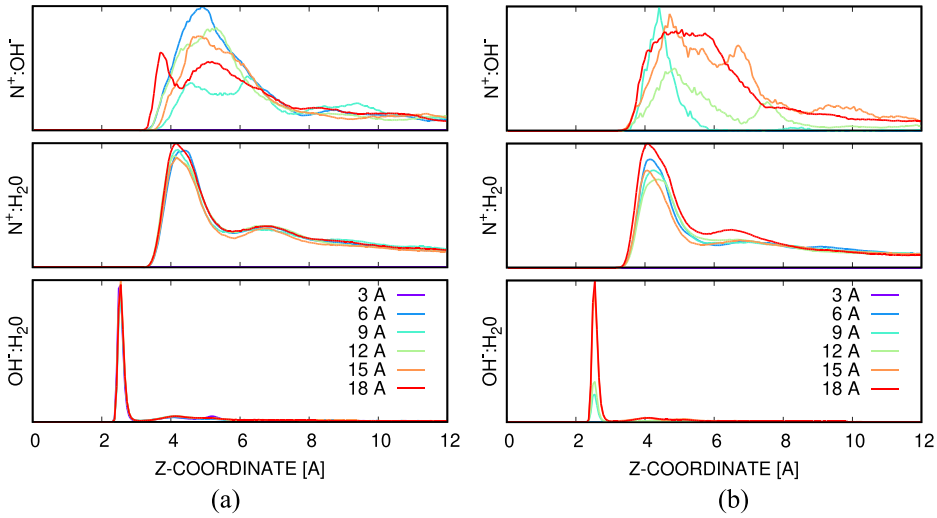

FIG. 9. Bare Ni electrode: radial distributions N^+:OH^-, N^+:H_2O, OH^-:H_2O as a function of distance from the electrode for surface charge (a) q = 0.0 and (b) q = −0.1 (e/atom). Radial distributions are computed for atoms in 3 Å wide regions starting at the electrode.

with H embedded in the oxide layer in direct association with an oxide O atom. These effects are, in large part, due to the differences in the unbiased point charges and induced charge distribution (refer to Fig. 6). Since oxides are dielectrics, they change local and long-range electric fields by screening due to induced and/or permanent dipoles.

At the same surface charges and comparable voltages to the simulation of the bare Ni region of the electrode discussed in Sec. IV B, we compute the electrolyte's response to electrical bias for a Ni electrode with a monolayer of NiO, as shown in Fig. 10. There are some similarities and noticeable differences in the profiles compared to the bare Ni case shown in Fig. 7. First, there is a larger counter charge density next to the electrode in the NiO-on-Ni case, which we can associate with the partially positively charged H in the increased density of surface water molecules. Examining the dipole density, the H-toward orientation is strong and barely shifts with increasing bias due to the strong, local polarization of the electrode itself. This near-surface dipole density is reflected in the electric potential which becomes constant but not zero in the far-field. This also leads to a lower effective voltage difference for the same surface charge, as expected with a dielectric layer. In addition, the more prominent positive dipole peak seen in Fig. 10 compared to Fig. 7 is apparently due to the dipole created by neighboring waters since no inversions of water molecules with the H toward the surface were observed.

Likewise, the concentration profiles shown in Fig. 11 are comparable to Fig. 8 but also display distinct differences. As in Fig. 8, the water density is uniform in the far-field and shows distinct signs of

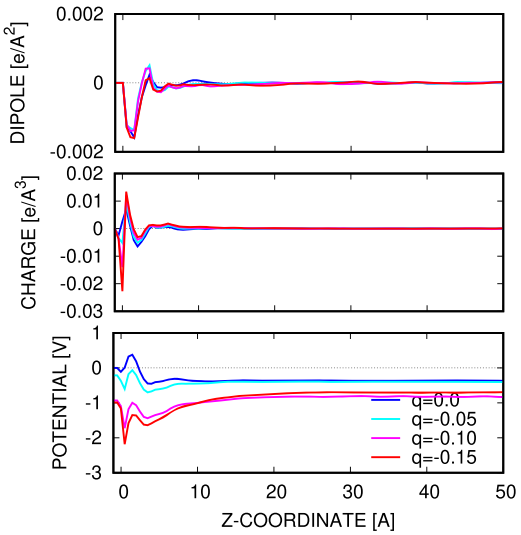

FIG. 10. Electrode with NiO monolayer: electrostatic potential, charge, and water dipole density profiles as a function of surface charge q (e/atom) on the electrode.

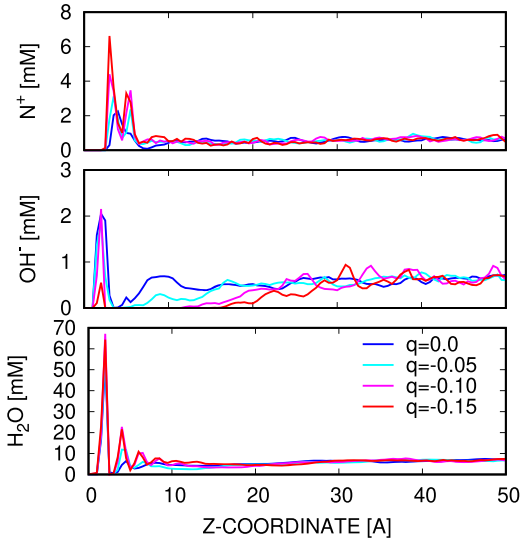

FIG. 11. Ni electrode with NiO monolayer: N^+, OH^-, and H_2O density profiles as a function of surface charge q (e/atom) on the electrode.

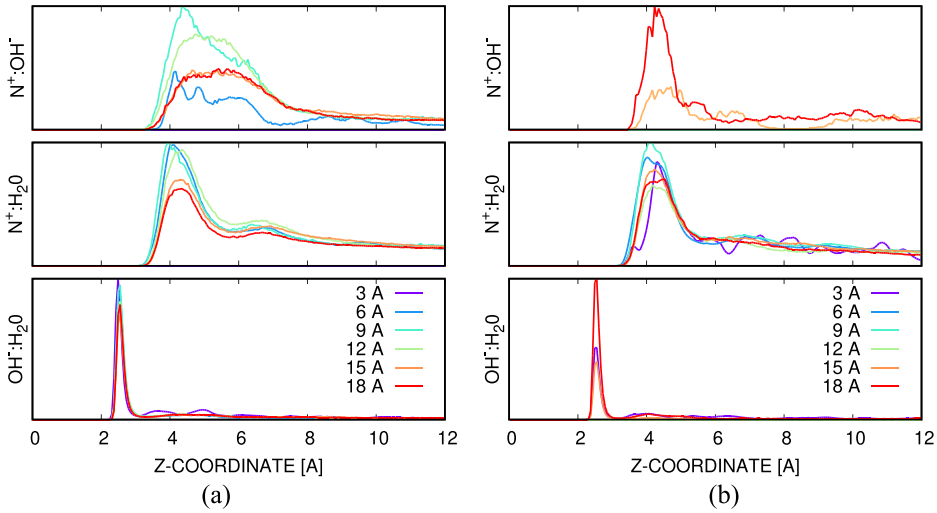

FIG. 12. Ni electrode with NiO monolayer: radial distributions N^+:OH^-, N^+:H_2O, OH^-:H_2O as a function of distance from the electrode for surface charge (a) q = 0.0 and (b) q = −0.1 (e/atom). Radial distributions are computed for atoms in 3 Å wide regions starting at the electrode. Note that the N^+:OH^- distribution for N^+ in the 0–3 Å region is not plotted due to a noisy, low count average.

structured layers near the electrode. On the other hand, the (time-averaged) water density at the electrode surface is much higher than in the bare metal case (approximately 40%, as corroborated by the snapshots shown in Fig. 3). Also, this spike in concentration is essentially unaffected by bias, a fact corroborated by nearly constant dipole density at the surface. Remarkably, significant OH^- remains associated with the electrode surface at high bias, but concentration decreases with increased bias (similar behavior has been observed in other systems[48]). Otherwise, the OH^- is similar to that for bare Ni, with a depletion zone increasing with increased bias and a nearly constant bulk concentration. The N^+ concentration is also similar to that for the bare Ni, shown in Fig. 8, but has a pronounced double peak near the interface. This feature is perhaps related to a significant residual OH^- concentration at the surface with bias.

The spatially binned RDFs shown in Fig. 12 are qualitatively similar to Fig. 9, implying that the electrode surface is not radically changing the coordination structures. There is a slight variation in OH^- and H_2O concentration at low bias which affects OH^-:H_2O and N^+:H_2O coordination that is not observed in Fig. 9. The presence of OH^- near the N^+ closest to the electrode in this case also appears in the N^+:OH^- RDF, but it is omitted in Fig. 9 due to sampling noise and an effort to maintain clarity. Also, in this case, the N^+:OH^- RDF clearly relaxes to bulk distribution at zero bias.

V. DISCUSSION

In response to the hypotheses H1–H5 posed in the work of Bates *et al.*[4] and reiterated in the Introduction, we find the following:

- Regarding H1, the electrical potential *is* altered by the ionomer and the oxide layer primarily due to dielectric effects of the immobile charges and their interplay with the mobile ones, as observed in Figs. 7 and 10. A significant concentration of positive charge from the ionomer lies near the surface of the electrode, as can be inferred from Figs. 8 and 11 and hence increases the potential.
- Regarding H2, the (negatively charged) HER electrode is *not* classical in the sense that there are no simple ions on the surface of the electrode defining the inner Helmholtz plane (IHP) since the positive charges are relatively immobile as part of the entangled and elastic ionomers. Also, the outer Helmholtz plane (OHP) is nebulous since the ionomer N^+ are coordinated with both OH^- and H_2O. Figures 9 and 12 indicate that solvation by the two species and hence the location of the OHP is changing with electrode bias voltage and, depending on the solvating species, ranges from 3 Å off the electrode surface to 15 Å. The coordination of water with N^+ is relatively insensitive to bias voltage, whereas a region depleted of the charged OH^- forms near the electrode with electrical bias and grows with increased bias. The dissociation of OH^- with N^+ appears to be governed by an energetic threshold. Since the N^+ are relatively immobile, there are significant N^+ atoms in the depletion region, but these near-electrode N^+ do respond elastically to the electrostatic forces and move closer to the electrode with increasing negative surface charge.
- Regarding H3, approximately 40% of the bare metal surface is coordinated with water molecules and this surface coverage almost doubles in areas covered by an oxide layer. So with modest oxide coverage, we *do* expect that the majority of the reactive sites to be occupied by water. This propensity seems to be facilitated by the ionomer not being adsorbed to the surface of the electrode.
- In addition, on the surface of the electrode, refer to Fig. 3, the proximity of the N^+ from the ionomer apparently displaces water and disrupts the tendency of the water to form ordered surface structures like rings, as in Ref. 33. From Figs. 8 and 11, it is clear that a significant concentration of the ionomer N^+ lies near the electrode surface.
- Regarding H4, the water molecules near the electrode surface orient in the manner dictated by the electric field (with O further away from the surface) in a mixture of either one or both hydrogens associated with surface atoms; however, in the surfaces with an oxide layer, the primary

association is with a surface oxygen and the configuration where one of the H legs of the water molecule lying on the electrode surface seems to dominate, as can be seen in Figs. 3 and 4. This hypothesis is *not* confirmed by our simulations.
- Regarding H5, nanoscale heterogeneity such as at the edge of an oxide region *does* provide local configurations favorable for water adsorption, as evidenced by the regions of high water coverage at the edge of the partially oxidized electrode in Figs. 3 and 4. This qualitative observation may corroborate how rough vs smooth electrodes exhibit qualitatively different reactivity; see Ref. 28 (Secs. 3.1 and 4.2) and the references therein.
- Also, the presence of a NiO monolayer apparently allows OH^- to remain near the electrode at high negative surface charges; compare Figs. 8 and 11.

So we find that H1, H3, and H5 are corroborated by the simulations, and H2 and H4 are not; however, H2 needs to be reinterpreted in light of the fact that the Helmholtz planes are not well-defined in this system.

Although we are presently unable to simulate the relevant reactions at the necessary time (molecular diffusion) and length (diffuse layer) scales, the fact that the reactions are fast compared with the processes MD represents well gives us some confidence that the results are representative of steady-state conditions. Also, the H_2 produced at the HER electrode is small and mobile, and not likely to affect the components of the electrolyte. In the future, hybrid treatment of the reacting interface with DFT and the diffuse layer with classical MD, such as the simulation of corrosion in silicon by Gleizer *et al.*,[56] should be possible. The consumption and production of species at the electrode will also necessitate an open boundary condition at the fictitious counter electrode. Finally, if positive ions are present, e.g., K^+ from dissolved KOH, they will likely adsorb to the electrode surface and hence screen the remainder of the electrolyte, having stronger effects on performance.

VI. CONCLUSION

We were able to simulate and examine the HER electrode-ionomer electrolyte interface with atomic detail using a combination of DFT and classical MD techniques. We observed configuration changes in response to external bias and the oxide coverage of the electrode. Information of this nature is relevant to the efficiency of the water splitting process. In particular, the concentration of the reactants, water, and the electric field at the interface have a direct relation to H_2 production.

In future work, we will explore in more detail the effect of surface roughness/nanostructuring and the presence of other phases, such as Cr_2O_3, on the HER electrode. Resolution of the dielectric field[57] may also shed light on the operation of these types of water splitting cells and give rise to more accurate and informative theories. Also, the entropic changes due to changes in pH discussed in Ref. 58 are likely correlated with the structural characterizations presented in this work, such as the spatial variation of radial distributions, and are another topic for potential future work.

ACKNOWLEDGMENTS

We would like to thank Norman Bartelt and Jeremy Templeton (Sandia) for insightful discussions on this work. This work was enabled by VASP (TU Vienna, https://www.vasp.at), LAMMPS (Sandia, https://lammps.sandia.gov), and Bader (Univ. Texas http://theory.cm.utexas.edu/henkelman/code/bader/). This work was supported by the U.S. Department of Energy, Office of Energy Efficiency and Renewable Energy (EERE), and specifically the Fuel Cell Technologies Office, Sandia National Laboratories, which is a multimission laboratory managed and operated by National Technology and Engineering Solutions of Sandia, LLC., a wholly owned subsidiary of Honeywell International, Inc., for the U.S. Department of Energy's National Nuclear Security Administration under Contract No. DE-NA0003525. The views expressed in the article do not necessarily represent the views of the U.S. Department of Energy or the United States Government.

REFERENCES

[1] S. Rahman and C. J. Andrews, Proc. IEEE **94**, 1781 (2006).
[2] N. R. Council, *The Hydrogen Economy: Opportunities, Costs, Barriers, and R&D Needs* (National Academies Press, 2004), https://www.nap.edu/read/10922/chapter/10.
[3] M. Navlani-García, K. Mori, Y. Kuwahara, and H. Yamashita, NPG Asia Mater. **10**, 277–292 (2018).
[4] M. K. Bates, Q. Jia, N. Ramaswamy, R. J. Allen, and S. Mukerjee, J. Phys. Chem. C **119**, 5467 (2015).
[5] M. Ünlü, D. Abbott, N. Ramaswamy, X. Ren, S. Mukerjee, and P. A. Kohl, J. Electrochem. Soc. **158**, B1423 (2011).
[6] R. Subbaraman, D. Tripkovic, D. Strmcnik, K.-C. Chang, M. Uchimura, A. P. Paulikas, V. Stamenkovic, and N. M. Markovic, Science **334**, 1256 (2011).
[7] D. Strmcnik, M. Uchimura, C. Wang, R. Subbaraman, N. Danilovic, D. Van Der Vliet, A. P. Paulikas, V. R. Stamenkovic, and N. M. Markovic, Nat. Chem. **5**, 300 (2013).
[8] N. Danilovic, R. Subbaraman, D. Strmcnik, K.-C. Chang, A. Paulikas, V. Stamenkovic, and N. M. Markovic, Angew. Chem. **124**, 12663 (2012).
[9] J.-S. Filhol and M. Neurock, Angew. Chem., Int. Ed. **45**, 402 (2006).
[10] R. Jinnouchi and A. B. Anderson, Phys. Rev. B **77**, 245417 (2008).
[11] E. Skúlason, V. Tripkovic, M. E. Björketun, S. Gudmundsdottir, G. Karlberg, J. Rossmeisl, T. Bligaard, H. Jónsson, and J. K. Nørskov, J. Phys. Chem. C **114**, 18182 (2010).
[12] E. Skúlason, G. S. Karlberg, J. Rossmeisl, T. Bligaard, J. Greeley, H. Jónsson, and J. K. Nørskov, Phys. Chem. Chem. Phys. **9**, 3241 (2007).
[13] G. Karlberg, T. Jaramillo, E. Skulason, J. Rossmeisl, T. Bligaard, and J. K. Nørskov, Phys. Rev. Lett. **99**, 126101 (2007).
[14] C. D. Taylor, S. A. Wasileski, J.-S. Filhol, and M. Neurock, Phys. Rev. B **73**, 165402 (2006).
[15] J. Rossmeisl, J. K. Nørskov, C. D. Taylor, M. J. Janik, and M. Neurock, J. Phys. Chem. B **110**, 21833 (2006).
[16] M. J. Janik, C. D. Taylor, and M. Neurock, J. Electrochem. Soc. **156**, B126 (2009).
[17] M. Otani, I. Hamada, O. Sugino, Y. Morikawa, Y. Okamoto, and T. Ikeshoji, J. Phys. Soc. Jpn. **77**, 024802 (2008).
[18] K. Chenoweth, A. C. Van Duin, and W. A. Goddard, J. Phys. Chem. A **112**, 1040 (2008).
[19] E. Spohr, Electrochim. Acta **44**, 1697 (1999).
[20] A. P. Willard, S. K. Reed, P. A. Madden, and D. Chandler, Faraday Discuss. **141**, 423 (2009).
[21] D. T. Limmer, A. P. Willard, P. Madden, and D. Chandler, Proc. Natl Acad. Sci. U. S. A. **110**, 4200 (2013).
[22] K.-Y. Yeh, M. J. Janik, and J. K. Maranas, Electrochim. Acta **101**, 308 (2013).

[23]Z. E. Hughes and T. R. Walsh, J. Colloid Interface Sci. **436**, 99 (2014).
[24]S. Dewan, V. Carnevale, A. Bankura, A. Eftekhari-Bafrooei, G. Fiorin, M. L. Klein, and E. Borguet, Langmuir **30**, 8056 (2014).
[25]D. T. Limmer, A. P. Willard, P. A. Madden, and D. Chandler, J. Phys. Chem. C **119**, 24016 (2015).
[26]K. Takae and A. Onuki, J. Chem. Phys. **143**, 154503 (2015).
[27]M. Foroutan, M. Darvishi, and S. M. Fatemi, Phys. Rev. E **96**, 033312 (2017).
[28]P. A. Thiel and T. E. Madey, Surf. Sci. Rep. **7**, 211 (1987).
[29]M. A. Henderson, Surf. Sci. Rep. **46**, 1 (2002).
[30]A. Hodgson and S. Haq, Surf. Sci. Rep. **64**, 381 (2009).
[31]J. Carrasco, A. Hodgson, and A. Michaelides, Nat. Mater. **11**, 667 (2012).
[32]E. M. Stuve, Chem. Phys. Lett. **519**, 1 (2012).
[33]S. Nie, P. J. Feibelman, N. Bartelt, and K. Thürmer, Phys. Rev. Lett. **105**, 026102 (2010).
[34]H. Helmholtz, Ann. Phys. **165**, 353 (1853).
[35]M. Gouy, J. Phys. Theor. Appl. **9**, 457 (1910).
[36]D. L. Chapman, London, Edinburgh Dublin Philos. Mag. J. Sci. **25**, 475 (1913).
[37]O. Stern, Z. Elektrochem. Angew. Phys. Chem. **30**, 508 (1924).
[38]C. Merlet, D. T. Limmer, M. Salanne, R. Van Roij, P. A. Madden, D. Chandler, and B. Rotenberg, J. Phys. Chem. C **118**, 18291 (2014).
[39]A. J. Bard, L. R. Faulkner, J. Leddy, and C. G. Zoski, *Electrochemical Methods: Fundamentals and Applications* (Wiley, New York, 1980), Vol. 2.
[40]J. N. Israelachvili, *Intermolecular and Surface Forces* (Academic Press, 2011).
[41]J. Newman and K. E. Thomas-Alyea, *Electrochemical Systems* (John Wiley & Sons, 2012).
[42]A. A. Kornyshev, J. Phys. Chem. B **117**(44), 13946 (2007).
[43]K. B. Oldham, J. Electroanal. Chem. **613**, 131 (2008).
[44]M. Z. Bazant, B. D. Storey, and A. A. Kornyshev, Phys. Rev. Lett. **106**, 046102 (2011).
[45]C. Gray and P. J. Stiles, Eur. J. Phys. **39**(5), 053002 (2018).
[46]J. W. Lee, R. H. Nilson, J. A. Templeton, S. K. Griffiths, A. Kung, and B. M. Wong, J. Chem. Theory Comput. **8**, 2012 (2012).
[47]J. W. Lee, J. A. Templeton, K. K. Mandadapu, and J. A. Zimmerman, J. Chem. Theory Comput. **9**, 3051 (2013).
[48]J. W. Lee, A. Mani, and J. A. Templeton, Langmuir **31**, 7496 (2015).
[49]A. D. MacKerell, Jr., D. Bashford, M. Bellott, R. L. Dunbrack, Jr., J. D. Evanseck, M. J. Field, S. Fischer, J. Gao, H. Guo, S. Ha *et al.*, J. Phys. Chem. B **102**, 3586 (1998).
[50]R. W. Hockney and J. W. Eastwood, *Computer Simulation Using Particles* (CRC Press, 1988).
[51]J. P. Perdew, K. Burke, and M. Ernzerhof, Phys. Rev. Lett. **77**, 3865 (1996).
[52]W. Tang, E. Sanville, and G. Henkelman, J. Phys.: Condens. Matter **21**, 084204 (2009).
[53]H. Heinz, R. Vaia, B. Farmer, and R. Naik, J. Phys. Chem. C **112**, 17281 (2008).
[54]P. Oliver, G. Watson, and S. Parker, Phys. Rev. B **52**, 5323 (1995).
[55]Reference 54 reports parameters for a Buckingham potential which we convert to a LJ parameterization by matching the potential well location and stiffness.
[56]A. Gleizer, G. Peralta, J. R. Kermode, A. De Vita, and D. Sherman, Phys. Rev. Lett. **112**, 115501 (2014).
[57]K. K. Mandadapu, J. A. Templeton, and J. W. Lee, J. Chem. Phys. **139**, 054115 (2013).
[58]J. Rossmeisl, K. Chan, E. Skúlason, M. E. Björketun, and V. Tripkovic, Catal. Today **262**, 36 (2016).